Improving the spatial resolution of effective elastic thickness estimation with the fan wavelet transform

J. F. Kirby[*1] and C. J. Swain[2]

[*] Corresponding author.

[1] Department of Spatial Sciences, Curtin University, GPO Box U1987, Perth, WA 6845, Australia. Tel: +61 8 9266 7701; fax: +61 8 9266 2703; email: j.kirby@curtin.edu.au.

[2] Department of Spatial Sciences, Curtin University, GPO Box U1987, Perth, WA 6845, Australia. Email: c_swain@wt.com.au.

Abstract

We show here a simple technique to improve the spatial resolution of the fan wavelet method for effective elastic thickness (T_e) estimation that we have previously developed. The technique involves reducing the number of significant oscillations within the Gaussian window of the Morlet wavelet from approximately five to three or fewer (while making an additional correction for its no-longer-zero mean value). Testing with synthetic models and data over South America indicates that the accompanying reduction in wavenumber resolution does not seriously affect the accuracy of the T_e estimates. Comparison against the more widely-used multitaper Fourier transform approach shows that the enhanced wavelet method not only improves upon the multitaper method's spatial resolution, but also is computationally much faster and requires the arbitrary variation of only one parameter compared to three for the multitaper method. Finally, we present a modified method to compute the predicted coherence using the multitaper method that, while not improving its spatial resolution, does improve the bias of recovered T_e estimates.

Keywords

Elastic thickness; Wavelets; Multitapers; South America.

1. Introduction

Since the mid 1990s, many spectral methods have been developed that are able to reveal spatial variations in the effective elastic thickness (T_e) of the lithosphere, whereas before only single estimates for a region were possible (e.g., Zuber et al., 1989). For example, Lowry and Smith (1994, 1995) applied the maximum entropy method (MEM) to the US Basin and Range province, Simons and van der Hilst (2002) used a multitaper Fourier transform in Australia (although they mapped the variations of coherence transition wavelength – see below), Braitenberg et al. (2002) used a space-domain convolution approach in the Alps, and Stark et al. (2003) developed a wavelet transform technique (based on Gaussian tensor wavelets) and applied it to southern Africa. Subsequently, Kirby and Swain (2004) developed an alternative wavelet method, this time based on superposed Morlet wavelets and called the 'fan' wavelet transform; this method has been applied to, for example, Australia (Swain and Kirby, 2006), and the Canadian shield (Audet and Mareschal, 2007).

All of the above-cited methods use variations of the coherence method of Forsyth (1985), in which the coherence between observed Bouguer gravity anomalies and topography is computed in the wavenumber (**k**) domain through:

$$\gamma^2\left(|\mathbf{k}|\right) = \frac{\left\langle GH^* \right\rangle \left\langle GH^* \right\rangle^*}{\left\langle GG^* \right\rangle \left\langle HH^* \right\rangle} \qquad (1)$$

where G and H are the tapered Fourier or wavelet transforms of Bouguer gravity anomaly and topography, respectively, the * indicates complex conjugation, and the angular brackets indicate an averaging process (see Kirby and Swain, 2009, for a discussion on averaging). This observed coherence is then compared against the predictions of a thin elastic plate model to find the best-fitting T_e. Theoretical Bouguer coherence curves have a characteristic shape, maintaining high values (close to 1) at long wavelengths, indicative of isostatic compensation, and low values (close to 0) at short, indicating mechanical support. At some "coherence transition" wavelength in between there is an often-sharp rollover from 1 to 0: the longer the wavelength of this rollover, the stronger the plate.

In the multitaper (MT) implementation, the study area is divided into overlapping windows of one, or a few, fixed window sizes, the coherence computed (via a multitaper Fourier transform) and inverted in each window. The resolution band is hence prescribed by, among other parameters, the choice of window size. The wavelet method, however, convolves a range of scaled wavelets with the *whole* data set to map and invert the coherence at each grid point. Hence the wavelet method, unlike the multitaper, should use the appropriate 'window' (i.e., scale) for the coherence transition wavelength at each point.

In this contribution we respond to criticism of the fan wavelet approach made by Pérez-Gussinyé et al. (2007, 2009a) that its lower spatial resolution than the multitaper method led to T_e features being over-smoothed. Both Pérez-Gussinyé et al. (2007) and Pérez-Gussinyé et al. (2009a) presented maps of South American T_e using the multitaper method which revealed short-wavelength T_e variations not resolved in

74 the fan wavelet-derived map of Tassara et al. (2007). Hence, we address this
75 acknowledged shortcoming by employing a Morlet wavelet of higher spatial
76 resolution in the fan wavelet transform. We also follow Kirby and Swain (2009) and
77 invert the square of the real part of the wavelet coherency, rather than the coherence,
78 because it is less sensitive to correlations between the initial loads on the plate, and to
79 "gravitational noise", both of which can cause incorrect recovery of T_e (Kirby and
80 Swain, 2009).
81
82 To demonstrate the improvement gained in using the complete Morlet wavelet, we
83 perform resolution and accuracy tests of the new method on synthetic data, and
84 compare these with results from application of the multitaper method.
85
86 **2. The wavelet transform**
87 **2.1 The fan wavelet transform**
88 The wavelet transform is a space-domain convolution of a signal with a wavelet, at a
89 series of scales. In the continuous wavelet transform (CWT), the scales are chosen
90 arbitrarily, but here we choose them to span a dyadic grid from the Nyquist
91 wavelength to the maximum dimension of the study area (e.g., Kirby, 2005). The
92 CWT is more readily computed in the wavenumber domain with the fast Fourier
93 transform. For a 2D space-domain (**x**) signal $g(\mathbf{x})$ with Fourier transform $G(\mathbf{k})$, its
94 wavelet coefficients are computed via:
95 $$\tilde{g}(s, \mathbf{x}, \theta) = \mathbf{F}^{-1}\left[G(\mathbf{k})\,\hat{\psi}_{s\theta}(\mathbf{k})\right] \quad (2)$$
96 where **k** is 2D wavenumber, s and θ are the scale and azimuth of the Morlet wavelet
97 respectively, $\hat{\psi}_{s\theta}(\mathbf{k})$ is the Fourier transform of the wavelet at a certain scale and
98 azimuth, and $\mathbf{F}^{-1}$ is the inverse 2D Fourier transform. The wavelet coefficients are

hence functions of position, scale and azimuth, with scale then converted to an equivalent Fourier wavenumber (see below). The wavelet coherency between two signals *g* and *h* is then computed from:

$$\Gamma(s,\mathbf{x}) = \frac{\left\langle \tilde{g}\,\tilde{h}^{*} \right\rangle_{\theta}}{\left\langle \tilde{g}\,\tilde{g}^{*} \right\rangle_{\theta}^{1/2} \left\langle \tilde{h}\,\tilde{h}^{*} \right\rangle_{\theta}^{1/2}} \tag{3}$$

which is complex-valued (Kirby and Swain, 2009). The averaging in Eq. (3) is performed over azimuth, at a particular scale, which gives isotropic coefficients if θ varies from 0° to 180° (Kirby, 2005). The coherence, Eq. (1), is thus the modulus-squared of the coherency, but as mentioned in the Introduction, we estimate T_e by inverting the squared-real-coherency ("SRC"), i.e., $(\mathrm{Re}\,\Gamma)^2$.

The fan wavelet transform of Kirby (2005) was developed in order to give wavelet coefficients that are both isotropic and complex. Isotropic coefficients are required to avoid an anisotropic bias on the estimate of T_e, while the coefficients must be complex-valued to preserve phase information. In contrast, other complex-valued 2D wavelets such as the Morlet wavelet give anisotropic wavelet coefficients, while isotropic wavelets such as the derivative of Gaussian family give real-valued wavelet coefficients. The fan wavelet transform is hence a series of rotated 2D Morlet wavelet coefficients spanning 180° that are then superposed for isotropy, while preserving their complex nature.

2.2 The complete Morlet wavelet

2D Morlet wavelets have the wavenumber domain equation:

$$\hat{\psi}(\mathbf{k}) = e^{-|\mathbf{k}-\mathbf{k}_0|^2/2} \tag{4}$$

where $\mathbf{k}_0 = (|\mathbf{k}_0|\cos\theta, |\mathbf{k}_0|\sin\theta)$, and θ is the resolving direction of the wavelet (e.g., Antoine et al., 2004). While the choice of the value of the central wavenumber, $|\mathbf{k}_0|$, of the Morlet wavelet is somewhat arbitrary, the value we have used in our previous work ($\pi\sqrt{2/\ln 2} \approx 5.336$) is standard throughout much of the wavelet literature, and gives a wavelet where the amplitude of the first sidelobes of the real part of the space-domain wavelet are a half that of the amplitude of the central peak (Addison, 2002) (see top-left panel of Fig. 1). If not actually using this specific value, all authors stipulate that $|\mathbf{k}_0| \geq 5$ in order for Eq. (4) to represent a valid wavelet. When $|\mathbf{k}_0| < 5$, the mean value of the wavelet in the space domain no longer approximates zero and thus does not satisfy the zero-mean requirement of wavelets (e.g., Antoine et al., 2004). This is evident from Eq. (4) for $|\mathbf{k}_0| = 3$, for example: at the zero wavenumber ($|\mathbf{k}| = 0$) the mother wavelet transform has a value of 0.01, a significant 'DC component'. In contrast, when $|\mathbf{k}_0| = 5.336$, its value here is $<10^{-6}$.

[FIG. 1]

However, allowing $|\mathbf{k}_0|$ to vary can be very useful for some applications. According to Addison (2002) and Addison et al. (2002), when $|\mathbf{k}_0|$ is relatively low, the Morlet wavelet gives a better resolution in the space-domain ("**x**-resolution") than for mid-range values ($|\mathbf{k}_0| \sim 5$), but therefore must give a worse resolution in the wavenumber domain ("**k**-resolution") from the uncertainty relation:

$$\Delta\mathbf{x}\,\Delta\mathbf{k} \geq 2\pi \qquad (5)$$

This improved **x**-resolution arises because, for a desired wavenumber (e.g., the coherence/SRC transition wavenumber), a $|\mathbf{k}_0| = 3.773$ wavelet is of a smaller scale (smaller spatial extent) than the corresponding $|\mathbf{k}_0| = 5.336$ wavelet needed to resolve

147 this particular wavenumber. This is shown in Fig. 1, where the wavelet scale has been
148 chosen so that the peak wavenumber (which gives the equivalent Fourier
149 wavenumber) is located at the Bouguer coherence transition wavenumber. When $|\mathbf{k}_0|$
150 has the lower value, the 'transition wavelet' (i.e., that wavelet whose equivalent
151 Fourier wavenumber (scale) corresponds to the coherence/SRC transition
152 wavenumber) has a smaller scale (giving it a better **x**-resolution), but a
153 commensurately larger bandwidth (giving it a worse **k**-resolution). Conversely, when
154 $|\mathbf{k}_0|$ is relatively high, the resulting wavelet coefficients have a poor **x**-resolution but a
155 good **k**-resolution. The larger the value of $|\mathbf{k}_0|$, the more the global scalogram tends
156 towards the periodogram estimate, though of course the spatial resolution decreases.
157
158 If a $|\mathbf{k}_0| < 5$ wavelet is desired, then the 'complete Morlet wavelet' must be used. In
159 the space domain the mother wavelet equation is:

160 $$\psi(\mathbf{x}) = \left(e^{i\mathbf{k}_0\cdot\mathbf{x}} - e^{-|\mathbf{k}_0|^2/2}\right)e^{-|\mathbf{x}|^2/2} \tag{6}$$

161 with Fourier transform:

162 $$\hat{\psi}(\mathbf{k}) = e^{-|\mathbf{k}-\mathbf{k}_0|^2/2} - e^{-\left(|\mathbf{k}|^2+|\mathbf{k}_0|^2\right)/2} \tag{7}$$

163 (Addison et al., 2002). The extra $\exp(-|\mathbf{k}_0|^2/2)$ terms in these equations correct for the
164 non-zero mean of the wavelet at small $|\mathbf{k}_0|$. In general, if the amplitude of the first
165 sidelobes is a fraction $1/p$ (where $p > 1$) of the amplitude of the central peak of the
166 space domain wavelet, then $|\mathbf{k}_0| = \pi\sqrt{2/\ln p}$. The values of $|\mathbf{k}_0|$ that we use in this
167 study are 2.668, 3.081, 3.773, 5.336 and 7.547, which give a space domain wavelet
168 whose first sidelobes are 1/16, 1/8, 1/4, 1/2, and $1/\sqrt{2}$ of the magnitude of the central
169 amplitude, respectively.
170

When the complete Morlet wavelet is to be used in a fan geometry, as in this study, the formula for the equivalent Fourier wavenumber (κ) at a certain wavelet scale (s) becomes the solution to the equation:

$$\kappa\left(1-e^{-s|\mathbf{k}_0|\kappa}\right)-\frac{|\mathbf{k}_0|}{s}=0 \tag{8}$$

which may be solved for κ using the Newton-Raphson method. However, when $|\mathbf{k}_0|$ = 2.668 (the smallest value we use here), the error in κ that is committed by using the approximation $\kappa = |\mathbf{k}_0|/s$ (Kirby, 2005) amounts to only 0.08%. A similar consequence applies to the angular separation between the Morlet wavelets, so we restrict our analyses to values of $|\mathbf{k}_0| \geq 2.668$. We have also confirmed that there is only a very minor bias to the wavelet spectra of fractal surfaces when using $|\mathbf{k}_0|$ = 2.668 compared to spectra from $|\mathbf{k}_0|$ = 5.336 (e.g., Kirby, 2005).

Finally, it is useful to derive an expression for the width of the wavelet in the space-domain, or "footprint". Since the Gaussian envelope never decays to zero, we define the footprint as space-domain width at half the wavelet's maximum amplitude. The Gaussian envelope of the daughter wavelet has the form $\psi_s(x) = \exp\left(-x^2/2s^2\right)$ from Eq. (6), so at half-maximum amplitude its width ($2x$) is:

$$\Delta_\psi = 2s\sqrt{2\ln 2} \tag{9}$$

Relating scale to an equivalent Fourier wavelength ($\lambda_e = 2\pi/\kappa = 2\pi s/|\mathbf{k}_0|$) we get:

$$\Delta_\psi = \lambda_e \frac{|\mathbf{k}_0|\sqrt{2\ln 2}}{\pi} \tag{10}$$

Eq. (10) hence gives the space-domain width of the wavelet needed to resolve an anomaly with wavelength λ_e. Remember though that the wavelet amplitude never

193 decays to zero and that it is convolved with all data in the study area; Eq. (10) merely
194 describes its primary region of influence.
195
196 **3. The multitaper method**
197 The multitaper (MT) method was introduced by Thomson (1982) in order to provide
198 better estimates of power spectra than those obtained by, for example, the
199 periodogram. The data are first multiplied by a set of orthogonal tapers in the space
200 domain, the Fourier transform of the data-taper product taken for each taper, and the
201 power spectrum determined at each taper. The final estimate of the signal's true
202 power spectrum is then the weighted average of the individual power spectra over all
203 tapers.
204
205 The tapers are designed to reduce spectral estimation bias and, because they are
206 orthogonal, combining them reduces the variance. Slepian (1978) introduced a set of
207 orthonormal tapers, discrete prolate spheroidal sequences, whose spectra comprise a
208 central lobe of halfwidth W, with sidelobes of decreasing amplitude. The ideal
209 spectrum is, of course, a delta function, i.e., a spike with no sidelobes. Hence,
210 decreasing W gives an increased resolution in the wavenumber-domain because the
211 taper spectrum tends towards a delta function, but this also results in increased
212 leakage between harmonics because the taper becomes broader in the space domain
213 (e.g., Simons et al., 2000).
214
215 The halfwidth of a taper is commonly expressed as the product NW, where N is the
216 number of data observations. (The halfwidth is actually $NW\Delta x$, where Δx is the space-
217 domain spacing of the gridded data.) For a given NW there are $k = 2NW - 1$ useful

tapers, where $2NW$ is the Shannon number, beyond which the tapers have greater leakage. As the order of the tapers increases, the number of oscillations in the space-domain increases, and in the wavenumber-domain the central lobe broadens and the number and amplitude of the sidelobes increases, resulting in a poorer wavenumber-domain resolution (e.g., Simons et al., 2000). However, using higher-order tapers is useful because the final estimation variance of the multitaper power spectrum decreases as $1/k$ (e.g., Simons et al., 2000, 2003; Prieto et al., 2007).

When applied to T_e estimation, the 2D MT Fourier transform must be used, giving k^2 tapers in total, i.e., k in each direction. McKenzie and Fairhead (1997) used $k = 3$ tapers, with $NW = 4$ (D. McKenzie, personal communication, 11 August 2010). Simons et al. (2000) applied the method to several regions within Australia using $k = 7$ and $NW = 4$. Swain and Kirby (2003) also analysed Australian T_e, though using $k = NW = 2$. In these studies, however, T_e was estimated within a single window. Alternatively, the spatial variations in T_e can be mapped by applying the multitaper method to many windows covering the study area. Pérez-Gussinyé et al. (2004) thus mapped T_e variations over Fennoscandia using $k = 3$ and 5, and $NW = 3$, and windows of size 1000×1000 km, and 1200×1200 km. The moving-window MT method was also applied to the Canadian Shield by Audet and Mareschal (2004), who used $k = NW = 3$, and windows of size 1024×1024 km. In more recent studies, Pérez-Gussinyé et al. (2007) used $k = 5$ and $NW = 3$, and windows of size 400×400 km, 600×600 km, and 800×800 km, while Pérez-Gussinyé et al. (2009a) used $k = NW = 3$, and windows of size 600×600 km, with both studies looking at South American T_e.

While small windows afford improved spatial resolution, they cannot capture large coherence transition wavelengths associated with high T_e values. The resulting downward bias in T_e estimates is reflected in Fig. 2 of Pérez-Gussinyé et al. (2009a). In this study we apply the MT method to synthetic data using $k = NW = 3$, and a window of size 400×400 km that is moved by the data grid spacing (i.e., every 20 km). This relatively small window size is chosen to test the spatial resolution limits of the MT method, when compared against the new complete Morlet wavelet method. We show below (Section 6.1) that a simple modification to the predicted coherence formula considerably reduces the resulting small-window bias.

4. Inversion for T_e

4.1 Wavelet transform

T_e is recovered from the Bouguer anomaly and topography using the wavelet transform method in the following manner. First, both datasets are mirrored about their edges prior to Fourier transformation, which, when used with the wavelet transform does not generally bias the results significantly, as it can with the periodogram method (Kirby and Swain, 2008). An observed SRC is then calculated from these data, then inverted using the "load-deconvolution" method of Forsyth (1985), whereby the initial loads are recreated assuming a starting T_e value in the thin elastic plate equations, and a predicted SRC determined (see the Appendix, and Swain and Kirby, 2006). In these synthetic experiments, we use the same crustal/mantle densities and depths as used in the synthetic model generation (Section 5). The minimum χ^2 misfit between observed and predicted SRC is found using Brent's method of minimisation (Press et al., 1992), with the inversion weighted using jackknife error estimates (Thomson and Chave, 1991). The T_e value corresponding to

the minimum χ^2 misfit is assigned to the grid node, and the procedure repeated for all grid nodes in the study area. The χ^2 misfit curves for a range of T_e values also yield an estimate of the error on T_e, represented by, for example, the 95% confidence limits (Press et al., 1992; Kirby and Swain, 2009). However, for visual clarity in the figures we do not show these limits here.

Note that the load-deconvolution method can also estimate the ratio between the initial internal and surface load amplitudes (the "loading ratio", f). Since this study focuses on T_e recovery we do not discuss estimation of f here, though the interested reader can find this in Kirby and Swain (2008, 2009).

4.2 Multitaper method

Inversion of the observed SRC for T_e using the MT method is approached in a slightly different manner, in that the data area is segmented into many overlapping windows, and the load deconvolution applied within each window. That is, the gravity and topography data are windowed, Fourier transformed, and the initial loads determined in the wavenumber domain from a starting T_e value. The MT and wavelet methods then depart in what happens next. In the MT approach, the initial load transforms must be inverse Fourier transformed back to the space domain, in order to be multiplied by the tapers, and then Fourier transformed back to the wavenumber domain, in order to compute the predicted SRC for the window (see the Appendix). These extra steps are necessary so that the same procedure that was applied to the data in order to compute an observed SRC is also applied to the predicted initial loads to compute a predicted SRC. If these measures are not taken, Pérez-Gussinyé et al.

(2004) found that biases between observed and predicted spectra arise, which then bias T_e estimates.

As for the wavelet approach, we find the minimum χ^2 misfit between observed and predicted SRC using Brent's method of minimisation (Press et al., 1992), with the inversion weighted using the analytical formula for coherence error (e.g., Bechtel et al., 1987). Again, we use the same crustal/mantle densities and depths as used in the synthetic model generation (Section 5). The T_e value corresponding to the minimum χ^2 misfit is assigned to the window, and the procedure repeated for all windows covering the study area. χ^2 confidence limits on T_e can also be computed (Section 4.1). As for the computation of observed MT SRC (Section 3), we use $k = NW = 3$, a window of size 400×400 km, with the windows moved by 20 km in both easting and northing.

In the Appendix we present an approach by which to improve T_e estimates from the multitaper method. Briefly, the new approach involves performing the load deconvolution on the observed gravity, rather than on its downward continued approximation to Moho relief. Results of this modification are presented in Section 6.1.

5. Synthetic models

The performance of any T_e-recovery method may be ascertained by applying it to various synthetic plate models with known T_e (e.g., Macario et al., 1995; Kirby and Swain, 2008). In our method, two random, fractal surfaces are generated using the method of Peitgen and Saupe (1988), using different random seeds for each, over an

area of 5100×5100 km, on a 20 km grid. Each surface has fractal dimension 2.5, and together act as the initial surface and internal loads upon a thin elastic plate. In all our synthetic models, the internal load is applied at a Moho of depth 35 km, and the crust comprises a single layer of density 2800 kg.m^{-3} overlying a mantle of density 3300 kg.m^{-3}. We also always assign the loading ratio, *f*, to be 1. The final Bouguer anomaly and topography after loading are then obtained by solving the flexural equation of a thin elastic plate. For plates with a uniform T_e distribution the flexural equation is solved using the Fourier transform, while for plates with a spatially-variable T_e distribution the method of finite differences is used (see Kirby and Swain, 2008).

This complete process is then repeated a further 99 times for the chosen $|\mathbf{k}_0|$ value using a different 'seed' in the random number generator each time. This gives different random, fractal load surfaces. After inversion of the 100 gravity/topography pairs, the resulting 100 T_e estimates are then averaged, in order to reduce the effect of random and unavoidable initial load correlations (Kirby and Swain, 2008).

6. Resolution and accuracy results from synthetic modelling

6.1 Variable-T_e plate

In order to demonstrate the increase in spatial resolution gained by using wavelets with a lower value of $|\mathbf{k}_0|$, we performed synthetic modelling using a plate with a spatially-variable T_e distribution. The model T_e is derived from a chirp signal, with spatially decreasing wavelength (Fig. 2a).

[FIG. 2]

[FIG. 3]

Figs 2b–f show the averaged T_e estimated from the SRC at different $|\mathbf{k}_0|$ values. As expected, the lower-$|\mathbf{k}_0|$ wavelets give a better space-domain T_e resolution than the higher-$|\mathbf{k}_0|$ wavelets, better defining the decreasing wavelength of the chirp signal. However, the T_e values of all the features in Fig. 2 are underestimated with respect to the input model, shown in the cross-sections in Fig. 3.

As discussed and explained by Kirby and Swain (2008), this arises because the fan wavelet method tends to underestimate relative T_e differences when the T_e-anomaly width is smaller than its coherence/SRC transition wavelength, and hence smaller than the footprint of the transition wavelet needed for its resolution (see Section 2.2 and Eq. (10)). Hence, when the transition wavelength is large (and T_e large), the transition wavelets will be large scale and the observed SRC will be spatially smoothed. Furthermore, high-$|\mathbf{k}_0|$ transition wavelets are spatially broader than their low-$|\mathbf{k}_0|$ counterparts (see Fig. 1), resulting in smoother observed SRCs, and a more underestimated relative T_e difference.

For a maximum T_e = 60 km with f = 1, as used here, the coherence/SRC transition wavelength is 419 km (Kirby and Swain, 2008). From Eq. (10) the transition wavelet footprint is 781 km at $|\mathbf{k}_0|$ = 7.547, but only 276 km at $|\mathbf{k}_0|$ =2.668, explaining the decrease in **x**-resolution for the higher-$|\mathbf{k}_0|$ wavelets as the chirp wavelength decreases (Fig. 3). The longest-wavelength chirp oscillation in the model is well-resolved by all $|\mathbf{k}_0|$ wavelets because its wavelength is ~1500 km, i.e., greater than their footprints and not too small to be averaged out. However, the smallest chirp wavelength is only 100 km, so here even the $|\mathbf{k}_0|$ =2.668 has trouble resolving it.

In the MT results the recovered resolution of the chirp oscillations is approximately comparable to the $|\mathbf{k}_0|$ = 3.081 or 3.773 results, though the amplitude is much reduced and biased downwards by ~12 km uniformly across the area (Figs 4a and 5). The resolution difference between the multitaper and $|\mathbf{k}_0|$ = 2.668 wavelet results at short chirp wavelengths (Fig. 5) can be explained by the larger multitaper window (400 km, compared to the wavelet footprint of 276 km) averaging over a greater area.

[FIG. 4]

[FIG. 5]

Of particular note is the correction of the downward T_e bias in the conventional approach (see the Appendix). As can be seen in Fig. 5, the conventional approach gives T_e values that have a ~12 km downward bias (green line in Fig. 5). However, by performing the load deconvolution using the observed gravity, rather than its downward continued expression, we recover the grid shown in Fig. 4b, shown as cross-section in Fig. 5 (red line). While not improving upon the spatial resolution, the new approach largely corrects for the 12 km underestimation of T_e. It gives a very similar correction to one based on Fig. 2a of Pérez-Gussinyé et al. (2009a,b) and assuming a uniform T_e of 35 km, which is its true average value.

6.2 Uniform-T_e plates

Synthetic modelling of a uniform-T_e plate eliminates the effect discussed in the previous section (i.e., large wavelet footprint vs narrow T_e anomalies) to give an unbiased accuracy assessment. We chose uniform-T_e plates with values ranging from

10 km to 150 km in intervals of 10 km. We also used five different $|\mathbf{k}_0|$ values for the wavelet method, but did not perform inversion using the MT method, since this has been done elsewhere (e.g., Pérez-Gussinyé et al., 2009a,b).

[FIG. 6]

Fig. 6 shows the results. As expected, the $|\mathbf{k}_0| = 7.547$ wavelet gives the most accurate results, because on a uniform plate with no T_e anomalies its poor **x**-resolution is irrelevant, while its good **k**-resolution is better able to resolve the transition wavelength than can wavelets with smaller $|\mathbf{k}_0|$ values. Conversely, the $|\mathbf{k}_0| = 2.668$ wavelet gives the worst T_e recovery, underestimating T_e by up to 23%. Note that the percentage underestimation remains relatively constant above model T_e values of 30 km.

It must be stressed, however, that the "calibration curves" in Fig. 6 represent the bias for a large (5100×5100 km) plate of uniform T_e. If T_e anomalies are narrow, or the study area smaller, then the downward bias to T_e will be more pronounced (Kirby and Swain, 2008). It is for this reason that we do not apply a correction to our T_e estimates based upon these calibration curves, as did Pérez-Gussinyé et al. (2009a,b) for the multitaper method.

Nevertheless, we note that even the $|\mathbf{k}_0| = 2.668$ curves in Fig. 6a give much less bias than the 400×400 km windows of the multitaper method, as shown in Fig. 2a of Pérez-Gussinyé et al. (2009b). We recognise, however, that implementation of our

new multitaper load deconvolution approach should improve upon the T_e estimates of Pérez-Gussinyé et al. (2009b).

7. South American T_e

To provide a real data example of the new method, Fig. 7 shows T_e computed over South America using $|\mathbf{k}_0|$ = 2.668 and 5.336 wavelets. The 5.336 result is almost identical to Fig. 3a of Tassara et al. (2007) (allowing for the different colour scales). Noticeable differences between the 2.668 and 5.336 results occur in the Guyana shield north of the Tacutu rift, and along the Transbrasiliano lineament.

[FIG. 7]

A criticism of the ($|\mathbf{k}_0|$ = 5.336) wavelet approach made by Pérez-Gussinyé et al. (2007) was that its lower resolution than their multitaper results led to T_e features in South America being smoothed out. The examples they cited were the low T_e along a substantial part of the Transbrasiliano lineament, the dyke swarms associated with the Paraná flood basalts, the Amazon basin, and the Tacutu rift. This criticism is, of course, valid for the 5.336 results, but is no longer so for the 2.668 results. A comparison of our Fig. 7a with Fig. 6a of Pérez-Gussinyé et al. (2009a) shows that the new wavelet method has succeeded in resolving very similar features in all these areas.

Although it is outside the scope of this paper, it should be noted that gravitational "noise" (McKenzie and Fairhead, 1997; McKenzie, 2003; Kirby and Swain, 2009) does exist over the continent, and casts doubt upon T_e values in some regions,

especially where we have recovered very high values. We return to this issue in the Conclusions.

8. Conclusions

We have shown how the fan wavelet method for T_e estimation may be improved to attain increased spatial resolution. Although this comes at the expense of a decreased wavenumber resolution, our synthetic modelling results show that this does not lead to significantly poorer T_e estimates. This refutes the arguments of Pérez-Gussinyé et al. (2007, 2009a) that the fan wavelet method inherently had poorer spatial resolution than the multitaper approach. Indeed, the wavelet method has significant advantages over the multitaper method. First, the fan wavelet method only requires the arbitrary variation of one parameter ($|\mathbf{k}_0|$), whereas the multitaper method requires the variation of three (window size, bandwidth and number of tapers). The fan wavelet method is also an order of magnitude computationally faster than the multitaper method because, as described in Section 4.2 and the Appendix, there are fewer arrays to store and fewer Fourier transforms to compute.

Second, the wavelet method allows for a more accurate estimation of T_e when using theoretical formulae. As Pérez-Gussinyé et al. (2004) demonstrated, observed coherences and admittances are increasingly biased as the window size decreases, due to spectral leakage, yet small windows are needed to resolve smaller T_e anomalies. This restriction presents no problems if a load-deconvolution approach is adopted, where predicted coherences/admittances are computed using windows of the same size, so that the leakage is the same for both observed and predicted quantities. However, theoretical coherence/admittance formulae are derived via the continuous

Fourier transform, which assumes an infinite data area without spectral leakage. So when observed, windowed coherences/admittances are compared with theoretical predictions, the resulting best-fit T_e will be biased. This is not the case for the wavelet transform if a large, (e.g., continent-sized) study area is chosen, because the wavelet method does not explicitly window the data. The resulting coherences/admittances have minimal bias when compared with theoretical coherence/admittance formulae (Kirby and Swain, 2004).

We have also reduced the downward bias of T_e estimates from the multitaper method, by performing the load deconvolution on gravity rather than Moho topography. This, however, does not improve the spatial resolution of the MT method, which remains slightly poorer than that of the wavelet transform approach with complete Morlet wavelets of low central wavenumber.

Finally, we provide some recommendations for $|\mathbf{k}_0|$ values. Owing to the better **k**-resolution, values of $|\mathbf{k}_0| > 5$ give more accurate absolute T_e estimates if the tectonic province is large and contains a relatively uniform T_e; in such cases, the low **x**-resolution of these wavelets is of less importance. If detailed T_e structure and/or accurate relative T_e differences are required, then values of $|\mathbf{k}_0| < 3.5$ are more likely to be useful, though the lower **k**-resolution of these wavelets could indicate greater uncertainty on the T_e estimates.

There remains, however, the issue of "gravitational noise" which can contaminate the Bouguer coherence and render load-deconvolution methods invalid (McKenzie, 2003; Kirby and Swain, 2009). This problem can occur in areas of subdued topography.

Although we do not show it here, we have found: 1) that such noise predominantly affects regions of the Earth where the coherence method indicates high T_e (Kirby and Swain, 2009); 2) that the size of the area affected increases as $|\mathbf{k}_0|$ decreases; and 3) that the lower **k**-resolution of low-$|\mathbf{k}_0|$ wavelets results in the noise spectrum being smeared over a larger bandwidth than with high-$|\mathbf{k}_0|$ wavelets. Hence, although low-$|\mathbf{k}_0|$ wavelets afford better spatial resolution, they are most useful when applied to the younger regions of the continents where T_e is more likely to be low.

The T_e estimation software is available at no cost as Fortran95 source code from the corresponding author.

Appendix. Load deconvolution

In the load deconvolution method of Forsyth (1985), initial surface and internal (i.e., within or at the base of the crust) loading processes may be considered separately, then superposed. The following equations are obtained in the Fourier domain. Consider two initial loads of geometric amplitude H_i and W_i applied at the surface and Moho (at depth z_m from sea level), respectively, of a thin elastic plate of known T_e. The initial surface load produces new surface topography H_T, and new Moho topography W_T. Similarly, the initial internal load produces new surface topography H_B, and new Moho topography W_B. The relationships between the final surface/Moho topographies and the initial loads are:

$$\begin{aligned} W_B &= \nu_B W_i \\ W_T &= \nu_T H_i \\ H_B &= \kappa_B W_i \\ H_T &= \kappa_T H_i \end{aligned} \qquad \text{(A1)}$$

where the wavenumber-dependent deconvolution coefficients are obtained from the solution to the thin elastic plate equations (Forsyth, 1985):

$$\begin{aligned} \nu_B &= 1 - \frac{\Delta\rho_2}{\Phi} \\ \nu_T &= -\frac{\Delta\rho_1}{\Phi} \\ \kappa_B &= -\frac{\Delta\rho_2}{\Phi} \\ \kappa_T &= 1 - \frac{\Delta\rho_1}{\Phi} \end{aligned} \tag{A2}$$

where $\Delta\rho_1 = \rho_c - \rho_f$, $\Delta\rho_2 = \rho_m - \rho_c$, ρ_c and ρ_m are crust (2800 kg.m^{-3}) and mantle (3300 kg.m^{-3}) densities, respectively, ρ_f is the density of the overlying fluid (air or water), and where:

$$\Phi = \frac{D|\mathbf{k}|^4}{g} + \rho_m - \rho_f \tag{A3}$$

D is flexural rigidity, $|\mathbf{k}|$ is the 1D wavenumber, g is the gravitational acceleration (9.8 ms^{-2}). The flexural rigidity (D) is related to the elastic thickness (T_e) by:

$$D = \frac{E T_e^3}{12\left(1-\sigma^2\right)} \tag{A4}$$

with E being Young's modulus (100 GPa), and σ being Poisson's ratio (0.25).

The total resultant surface topography, H, if both processes act together will be $H = H_T + H_B$, while the net Moho topography $W = W_T + W_B$. For combined surface and internal loading, the initial loads are related to the final, predicted Moho and surface topographies after flexure (W and H, respectively) by a matrix equation:

$$\begin{pmatrix} W \\ H \end{pmatrix} = \begin{pmatrix} \nu_B & \nu_T \\ \kappa_B & \kappa_T \end{pmatrix} \begin{pmatrix} W_i \\ H_i \end{pmatrix} \tag{A5}$$

[c.f. Eq. (18) of Forsyth (1985)].

530

531 In Forsyth (1985)'s original method, the observed Moho topography (W) is

532 determined from the observed Bouguer gravity anomaly (G) using the relationship:

533 $$W = \frac{G\, e^{|\mathbf{k}|z_m}}{2\pi \mathcal{G} \Delta\rho_2} \qquad \text{(A6)}$$

534 where $\mathcal{G}$is the Newtonian gravitational constant (Parker, 1972). A predicted

535 coherence (for an assumed T_e) is then determined by substitution of $H = H_T + H_B$, $W =$

536 $W_T + W_B$ and Eq. (A6) into the coherence formula, Eq. (1), though here we use the

537 predicted coherency [c.f., Eq. (3)]:

538 $$\Gamma_p^{(W)}\left(|\mathbf{k}|\right) = \frac{\left\langle W_T H_T^* + W_B H_B^* \right\rangle_{|\mathbf{k}|}}{\left\langle W_T W_T^* + W_B W_B^* \right\rangle_{|\mathbf{k}|}^{1/2} \left\langle H_T H_T^* + H_B H_B^* \right\rangle_{|\mathbf{k}|}^{1/2}} \qquad \text{(A7)}$$

539 where $\langle\cdot\rangle_{|\mathbf{k}|}$ indicates averaging over annuli of equal wavenumber (though see

540 discussion below), and Forsyth (1985) assumed that $\left\langle \exp(-\mathbf{k}z_m) W(\mathbf{k}) \right\rangle_{|\mathbf{k}|} =$

541 $\exp(-|\mathbf{k}|z_m)\left\langle W(\mathbf{k})\right\rangle_{|\mathbf{k}|}$, so that the exponential terms cancel. Forsyth (1985) also

542 assumed that the surface and internal loading processes are independent, or

543 statistically uncorrelated. This restriction is expressed by setting the average of terms

544 containing both surface ($_T$) and internal ($_B$) loads to zero, e.g., $\left\langle W_T H_B^* \right\rangle = 0$, etc.

545

546 Eq. (A7) is the formula used by the MT method for predicted coherency computation,

547 though the averaging is also performed over the tapers, and then over wavenumber

548 annuli.

549

550 An alternative approach is to compute the surface and internal loading components of
551 the Bouguer anomaly, rather than Moho topography. In this fashion, we have:

552
$$\begin{aligned} G_B &= \mu_B W_i \\ G_T &= \mu_T H_i \\ H_B &= \kappa_B W_i \\ H_T &= \kappa_T H_i \end{aligned} \tag{A8}$$

553 where the wavenumber-dependent gravity deconvolution coefficients are:

554
$$\begin{aligned} \mu_B &= \frac{2\pi\mathcal{G}\Delta\rho_2}{\Phi}\left(\Phi - \Delta\rho_2\right)e^{-|\mathbf{k}|z_m} = 2\pi\mathcal{G}\Delta\rho_2 e^{-|\mathbf{k}|z_m}\nu_B \\ \mu_T &= \frac{-2\pi\mathcal{G}\Delta\rho_1}{\Phi}\Delta\rho_2 e^{-|\mathbf{k}|z_m} = 2\pi\mathcal{G}\Delta\rho_2 e^{-|\mathbf{k}|z_m}\nu_T \end{aligned} \tag{A9}$$

555 and the expressions for κ_B and κ_T in Eq. (A2) do not change. The total resultant
556 surface topography, H, if both processes act together will be $H = H_T + H_B$, while the
557 net Bouguer anomaly is $G = G_T + G_B$. For combined surface and internal loading, the
558 initial loads are related to the final, predicted Bouguer anomaly and surface
559 topography after flexure by:

560
$$\begin{pmatrix} G \\ H \end{pmatrix} = \begin{pmatrix} \mu_B & \mu_T \\ \kappa_B & \kappa_T \end{pmatrix}\begin{pmatrix} W_i \\ H_i \end{pmatrix} \tag{A10}$$

561 The predicted coherency is then:

562
$$\Gamma_p^{(G)}\left(|\mathbf{k}|\right) = \frac{\left\langle G_T H_T^* + G_B H_B^* \right\rangle_{|\mathbf{k}|}}{\left\langle G_T G_T^* + G_B G_B^* \right\rangle_{|\mathbf{k}|}^{1/2}\left\langle H_T H_T^* + H_B H_B^* \right\rangle_{|\mathbf{k}|}^{1/2}} \tag{A11}$$

563

564 In theory, Eqs (A7) and (A11) should give identical predicted coherencies. However,
565 in practice they do not (as shown in Figs 4 and 5). If Eqs (A1), (A5) and (A6) are
566 substituted into Eq. (A7) we obtain the predicted coherency as computed by
567 deconvolution using Moho topography:

568 $$\Gamma_p^{(W)}\left(|\mathbf{k}|\right)=\frac{\left\langle e^{2|\mathbf{k}|z_m}\Delta_W^{-2}\left(\nu_T\kappa_T\ \eta\eta^*+\nu_B\kappa_B\ \zeta\zeta^*\right)\right\rangle_{|\mathbf{k}|}}{\left\langle e^{2|\mathbf{k}|z_m}\Delta_W^{-2}\left(\nu_T^2\ \eta\eta^*+\nu_B^2\ \zeta\zeta^*\right)\right\rangle_{|\mathbf{k}|}^{1/2}\left\langle e^{2|\mathbf{k}|z_m}\Delta_W^{-2}\left(\kappa_T^2\ \eta\eta^*+\kappa_B^2\ \zeta\zeta^*\right)\right\rangle_{|\mathbf{k}|}^{1/2}} \quad \text{(A12)}$$

569 where $\Delta_W = \nu_B\kappa_T-\nu_T\kappa_B$ is the determinant from Eq. (A5); $\eta = -\kappa_B G+Ae^{-|\mathbf{k}|z_m}\nu_B H$;

570 and $\zeta = \kappa_T G-Ae^{-|\mathbf{k}|z_m}\nu_T H$. The expression when the gravity-deconvolution method is

571 used is obtained by substituting Eqs (A8) and (A10) into Eq. (A11), and rearranging

572 to match Eq. (A12) as best as possible:

573 $$\Gamma_p^{(G)}\left(|\mathbf{k}|\right)=\frac{\left\langle e^{|\mathbf{k}|z_m}\Delta_W^{-2}\left(\nu_T\kappa_T\ \eta\eta^*+\nu_B\kappa_B\ \zeta\zeta^*\right)\right\rangle_{|\mathbf{k}|}}{\left\langle \Delta_W^{-2}\left(\nu_T^2\ \eta\eta^*+\nu_B^2\ \zeta\zeta^*\right)\right\rangle_{|\mathbf{k}|}^{1/2}\left\langle e^{2|\mathbf{k}|z_m}\Delta_W^{-2}\left(\kappa_T^2\ \eta\eta^*+\kappa_B^2\ \zeta\zeta^*\right)\right\rangle_{|\mathbf{k}|}^{1/2}} \quad \text{(A13)}$$

574 Comparison of Eqs (A12) and (A13) shows that the former has extra terms of

575 $\exp\left(|\mathbf{k}|z_m\right)$ and $\exp\left(2|\mathbf{k}|z_m\right)$. If the annuli were narrow enough to assume but one

576 value of |**k**| then these terms could be taken out of the averaging brackets and would

577 cancel, making Eqs (A12) and (A13) identical. However, this does not occur in most

578 practical implementations, and the exponential terms become prohibitively large,

579 biasing the predicted coherency and hence recovered T_e.

580

581 The fan wavelet method is based on a further development of Eq. (A11) which greatly

582 improves computation time. If Eqs (A8) are substituted into Eq. (A11), we get:

583 $$\Gamma_p^{(G)}\left(|\mathbf{k}|\right)=\frac{\left\langle \mu_T\kappa_T\left|H_i\right|^2+\mu_B\kappa_B\left|W_i\right|^2\right\rangle_{|\mathbf{k}|}}{\left\langle \mu_T^2\left|H_i\right|^2+\mu_B^2\left|W_i\right|^2\right\rangle_{|\mathbf{k}|}^{1/2}\left\langle \kappa_T^2\left|H_i\right|^2+\kappa_B^2\left|W_i\right|^2\right\rangle_{|\mathbf{k}|}^{1/2}} \quad \text{(A14)}$$

584 as the Fourier transform expression. But with the wavelet transform the deconvolution

585 coefficients can be taken outside the averaging brackets, because the averaging is

586 performed over the wavelet azimuth and these coefficients are functions of wavelet

scale (equivalent Fourier wavenumber) only. So, in terms of the wavelet transform, Eq. (A14) becomes:

$$\Gamma_p^{(WT)}(s,\mathbf{x}) = \frac{\mu_T \kappa_T \left\langle \left|\tilde{h}_i\right|^2 \right\rangle_\theta + \mu_B \kappa_B \left\langle \left|\tilde{w}_i\right|^2 \right\rangle_\theta}{\left[\mu_T^2 \left\langle \left|\tilde{h}_i\right|^2 \right\rangle_\theta + \mu_B^2 \left\langle \left|\tilde{w}_i\right|^2 \right\rangle_\theta\right]^{1/2} \left[\kappa_T^2 \left\langle \left|\tilde{h}_i\right|^2 \right\rangle_\theta + \kappa_B^2 \left\langle \left|\tilde{w}_i\right|^2 \right\rangle_\theta\right]^{1/2}} \quad \text{(A15)}$$

for $\tilde{h}_i(s,\mathbf{x},\theta)$ and $\tilde{w}_i(s,\mathbf{x},\theta)$. Now we can make use of the loading ratio, *f*, introduced by Forsyth (1985), which, for the wavelet transform, is computed through:

$$f^2(s,\mathbf{x}) = \frac{\left\langle \left|\tilde{w}_i\right|^2 \right\rangle_\theta}{r^2 \left\langle \left|\tilde{h}_i\right|^2 \right\rangle_\theta} \quad \text{(A16)}$$

where we define $r = \Delta\rho_1/\Delta\rho_2$. So dividing numerator and denominator of Eq. (A15) by $\left\langle \left|\tilde{h}_i\right|^2 \right\rangle_\theta$ we find:

$$\Gamma_p(s,\mathbf{x}) = \frac{\mu_T \kappa_T + \mu_B \kappa_B f^2 r^2}{\left[\mu_T^2 + \mu_B^2 f^2 r^2\right]^{1/2} \left[\kappa_T^2 + \kappa_B^2 f^2 r^2\right]^{1/2}} \quad \text{(A17)}$$

This demonstrates why the wavelet method is much faster than the multitaper method. In the wavelet method, only $\tilde{h}_i(s,\mathbf{x},\theta)$ and $\tilde{w}_i(s,\mathbf{x},\theta)$ need be computed from the observed gravity and topography data at a given T_e, and averaging is performed over azimuth only. In the multitaper method, however, four grids [$H_T(\mathbf{k})$, $H_B(\mathbf{k})$, $G_T(\mathbf{k})$, and $G_B(\mathbf{k})$] must be computed at a given T_e, then averaged over both wavenumber annuli and the multitapers.

Acknowledgements. We thank Martin Schimmel for useful discussion, Marta Pérez-Gussinyé for the South American province boundaries, and the two anonymous reviewers for their constructive suggestions. The figures were plotted using GMT

606 (Wessel and Smith, 1998). This work was supported by ARC grant DP0878453, and
607 is TIGeR publication number 232.
608
609 **References**
610 Addison, P. S., 2002. The Illustrated Wavelet Transform Handbook, Institute of
611 Physics Publishing, Bristol, UK, 353pp.
612 Addison, P. S., Watson, J. N., Feng, T., 2002. Low-oscillation complex wavelets,
613 Journal of Sound Vibration 254, 733-762.
614 Antoine, J.-P., Murenzi, R., Vandergheynst, P., Ali, S. T., 2004. Two-dimensional
615 Wavelets and their Relatives, Cambridge University Press, Cambridge, UK, 458pp.
616 Audet, P., Mareschal, J.-C., 2004. Anisotropy of the flexural response of the
617 lithosphere in the Canadian Shield, Geophysical Research Letters 31(20), L20601,
618 doi:10.1029/2004GL021080.
619 Audet, P., Mareschal, J.-C., 2007. Wavelet analysis of the coherence between
620 Bouguer gravity and topography: application to the elastic thickness anisotropy in
621 the Canadian Shield, Geophysical Journal International 168, 287-298.
622 Banks, R. J., Francis, S. C., Hipkin, R. G., 2001. Effects of loads in the upper crust on
623 estimates of the elastic thickness of the lithosphere, Geophysical Journal
624 International 145, 291-299.
625 Bassin, C., Laske, G., Masters, G., 2000. The current limits of resolution for surface
626 wave tomography in North America, EOS Transactions of the American
627 Geophysical Union 81, F897.
628 Bechtel, T. D., Forsyth, D. W., Swain, C. J., 1987. Mechanisms of isostatic
629 compensation in the vicinity of the East African Rift, Kenya, Geophysical Journal of
630 the Royal Astronomical Society 90, 445-465.

631 Braitenberg, C., Ebbing, J., Götze, H.-J., 2002. Inverse modelling of elastic thickness
632 by convolution method - the Eastern Alps as a case example, Earth and Planetary
633 Science Letters 202, 387-404.
634 Forsyth, D. W., 1985. Subsurface loading and estimates of the flexural rigidity of
635 continental lithosphere, Journal of Geophysical Research 90(B14), 12,623-12,632.
636 Kirby, J. F., 2005. Which wavelet best reproduces the Fourier power spectrum?
637 Computers and Geosciences 31(7), 846-864.
638 Kirby, J. F., Swain, C. J., 2004. Global and local isostatic coherence from the wavelet
639 transform, Geophysical Research Letters 31(24), L24608,
640 doi:10.1029/2004GL021569.
641 Kirby, J. F., Swain, C. J., 2008. An accuracy assessment of the fan wavelet coherence
642 method for elastic thickness estimation, Geochemistry Geophysics Geosystems 9(3),
643 Q03022, doi:10.1029/2007GC001773, (Correction, Geochemistry Geophysics
644 Geosystems 9(5), Q05021, doi:10.1029/2008GC002071, 2008).
645 Kirby, J. F., Swain, C. J., 2009. A reassessment of spectral T_e estimation in
646 continental interiors: the case of North America, Journal of Geophysical Research
647 114(B8), B08401, doi:10.1029/2009JB006356.
648 Lowry, A. R., Smith, R. B., 1994. Flexural rigidity of the Basin and Range–Colorado
649 Plateau–Rocky Mountain transition from coherence analysis of gravity and
650 topography, Journal of Geophysical Research 99(B10), 20,123-20,140.
651 Lowry, A. R., Smith, R. B., 1995. Strength and rheology of the western U.S.
652 Cordillera, Journal of Geophysical Research 100(B9), 17,947-17,963.
653 Macario, A., Malinverno, A., Haxby, W. F., 1995. On the robustness of elastic
654 thickness estimates obtained using the coherence method, Journal of Geophysical
655 Research 100(B8), 15,163-15,172.

McKenzie, D., 2003. Estimating T_e in the presence of internal loads, Journal of Geophysical Research 108(B9), 2438, doi:10.1029/2002JB001766.

McKenzie, D., Fairhead, J. D., 1997. Estimates of the effective elastic thickness of the continental lithosphere from Bouguer and free air gravity anomalies, Journal of Geophysical Research 102(B12), 27,523-27,552.

Parker, R. L., 1972. The rapid calculation of potential anomalies, Geophysical Journal of the Royal Astronomical Society 31, 447-455.

Peitgen, H.-O., Saupe, D., 1988. The Science of Fractal Images, Springer, New York, 312pp.

Pérez-Gussinyé, M., Lowry, A. R., Watts, A. B., Velicogna, I., 2004. On the recovery of effective elastic thickness using spectral methods: Examples from synthetic data and from the Fennoscandian Shield, Journal of Geophysical Research 109(B10), B10409, doi:10.1029/2003JB002788.

Pérez-Gussinyé, M., Lowry, A. R., Watts, A. B., 2007. Effective elastic thickness of South America and its implications for intracontinental deformation, Geochemistry Geophysics Geosystems 8(5), Q05009, doi:10.1029/2006GC001511.

Pérez-Gussinyé, M., Swain, C. J., Kirby, J. F., Lowry, A. R., 2009a. Spatial variations of the effective elastic thickness, T_e, using multitaper spectral estimation and wavelet methods: Examples from synthetic data and application to South America, Geochemistry, Geophysics, Geosystems 10(4), Q04005, doi:10.1029/2008GC002229.

Pérez-Gussinyé, M., Metois, M., Fernández, M., Vergés, J., Fullea, J., Lowry, A. R., 2009b. Effective elastic thickness of Africa and its relationship to other proxies for lithospheric structure and surface tectonics, Earth and Planetary Science Letters 287, 152-167.

Press, W. H., Teukolsky, S. A., Vetterling, W. T., Flannery, B. P., 1992. Numerical Recipes in Fortran 77, 2nd Ed., Cambridge University Press, Cambridge, 933pp.

Prieto, G. A., Parker, R. L., Thomson, D. J., Vernon, F. L., Graham, R. L., 2007. Reducing the bias of multitaper spectrum estimates, Geophysical Journal International 171, 1269-1281.

Simons, F. J., Zuber, M. T., Korenaga, J., 2000. Isostatic response of the Australian lithosphere: Estimation of effective elastic thickness and anisotropy using multitaper spectral analysis, Journal of Geophysical Research 105(B8), 19,163-19,184.

Simons, F.J., van der Hilst, R. D., 2002. Age-dependent seismic thickness and mechanical strength of the Australian lithosphere, Geophysical Research Letters 29(11), doi:10.1029/2002GL014962.

Simons, F. J., van der Hilst, R. D., Zuber, M. T., 2003. Spatiospectral localization of isostatic coherence anisotropy in Australia and its relation to seismic anisotropy: Implications for lithospheric deformation, Journal of Geophysical Research 108(B5), 2250, doi:10.1029/2001JB000704.

Slepian, D., 1978. Prolate spheroidal wave functions, Fourier analysis, and uncertainty – V: the discrete case, Bell System Technical Journal 57(5), 1371-1430.

Stark, C. P., Stewart, J., Ebinger, C. J., 2003. Wavelet transform mapping of effective elastic thickness and plate loading: Validation using synthetic data and application to the study of southern African tectonics, Journal of Geophysical Research 108(B12), 2558, doi:10.1029/2001JB000609.

Swain, C. J., Kirby, J. F., 2003. The effect of 'noise' on estimates of the elastic thickness of the continental lithosphere by the coherence method, Geophysical Research Letters 30(11), 1574, doi:10.1029/2003GL017070.

Swain, C. J., Kirby, J. F., 2006. An effective elastic thickness map of Australia from wavelet transforms of gravity and topography using Forsyth's method, Geophysical Research Letters 33(2), L02314, doi:10.1029/2005GL025090.

Tassara, A., Swain, C. J., Hackney, R. I., Kirby, J. F., 2007. Elastic thickness structure of South America estimated using wavelets and satellite-derived gravity data, Earth and Planetary Science Letters 253, 17-36.

Thomson, D. J., 1982. Spectrum estimation and harmonic-analysis, Proceedings of the IEEE 70(9), 1055-1096.

Thomson, D. J., Chave, A. D., 1991. Jackknifed error estimates for spectra, coherences, and transfer functions, In: Haykin, S. (Ed.) Advances in Spectrum Analysis and Array Processing 1(2), Prentice Hall, Englewood Cliffs, NJ, pp. 58-113.

Wessel, P., Smith, W. H. F., 1998. New, improved version of Generic Mapping Tools released, EOS Transactions of the American Geophysical Union 79(47), 579.

Zuber, M. T., Bechtel, T. D., Forsyth, D. W., 1989. Effective elastic thickness of the lithosphere and the mechanisms of isostatic compensation in Australia, Journal of Geophysical Research 94(B7), 9353-9367.

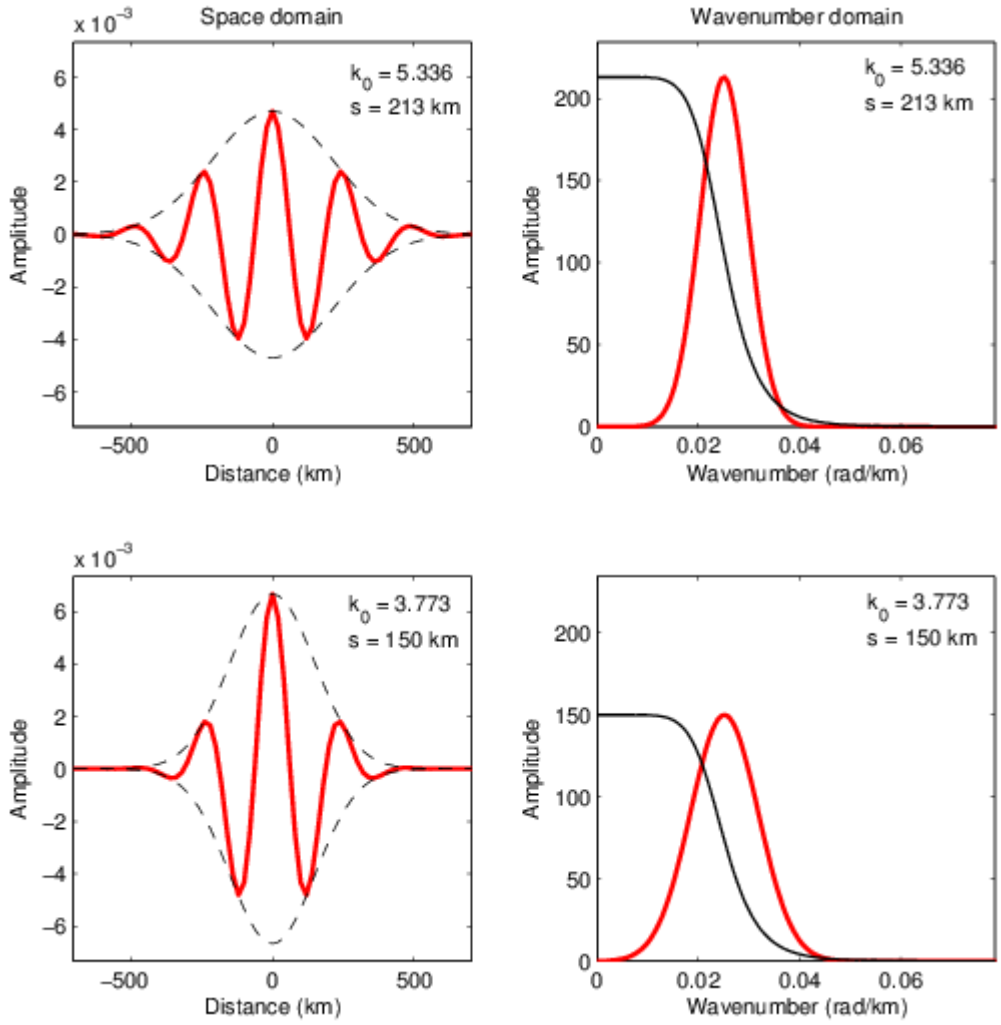

Fig. 1. Cross-sections through 2-D complete Morlet wavelets (red lines) in the space domain (real part, left-hand panels), and wavenumber domain (right-hand panels). Top row shows the wavelet at $|\mathbf{k}_0| = 5.336$ and a scale of 213 km; bottom row shows the wavelet at $|\mathbf{k}_0| = 3.773$ and a scale of 150 km. The black line in the wavenumber domain plots is the coherence/SRC for $T_e = 20$ km and $f = 1$, scaled to the maximum amplitude of the wavenumber domain wavelet for visual clarity. Hence, these wavelets are transition wavelets.

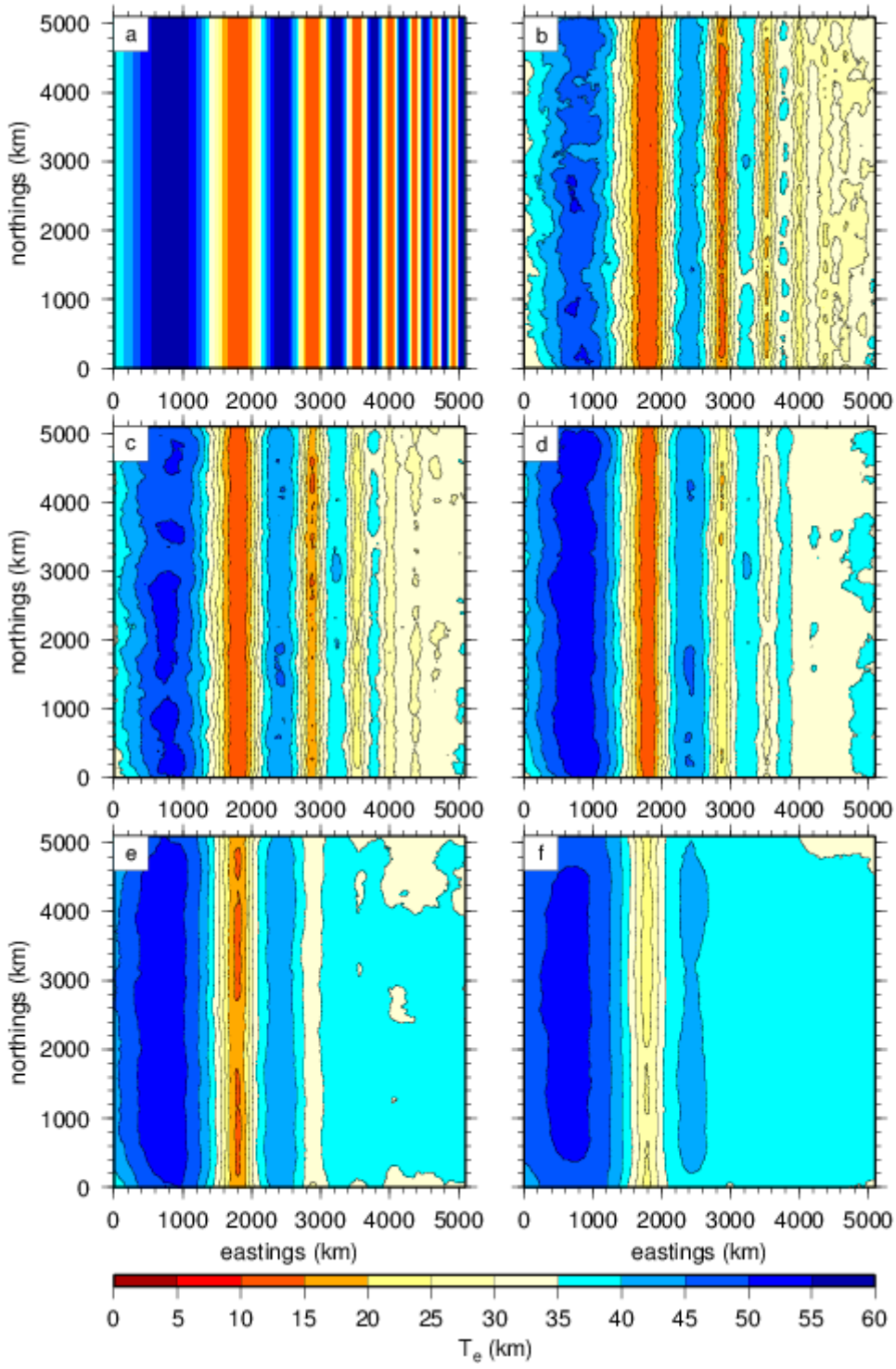

Fig. 2. T_e averaged over 100 T_e estimates recovered using the wavelet transform from 100 synthetic load pairs emplaced on a plate with the T_e distribution shown in (a), which is a chirp signal with peak-to-peak T_e amplitude of 50 km, and mean value 35 km. The following $|\mathbf{k}_0|$ values were used: (b) 2.668, (c) 3.081, (d) 3.773, (e) 5.336, and (f) 7.547. T_e contours in (b)-(f) at 5 km intervals.

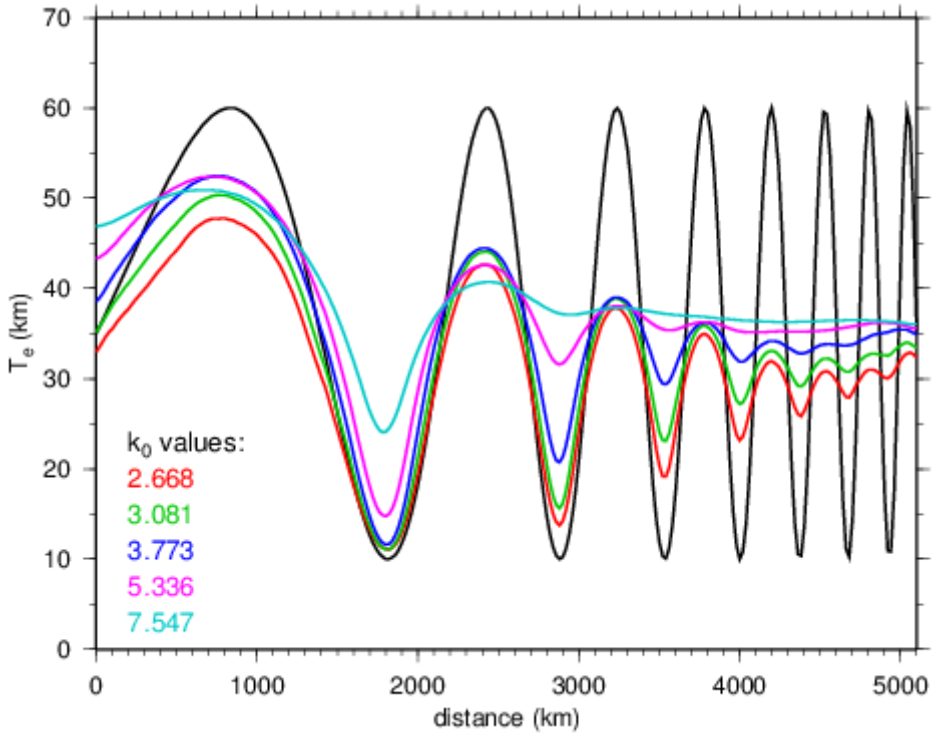

739

740 Fig. 3. Average T_e from west to east of the input T_e distribution in Fig. 2a (black), and

741 the wavelet T_e grids in Figs 2b-f, for the indicated $|\mathbf{k}_0|$ values. That is, values of

742 constant easting are averaged.

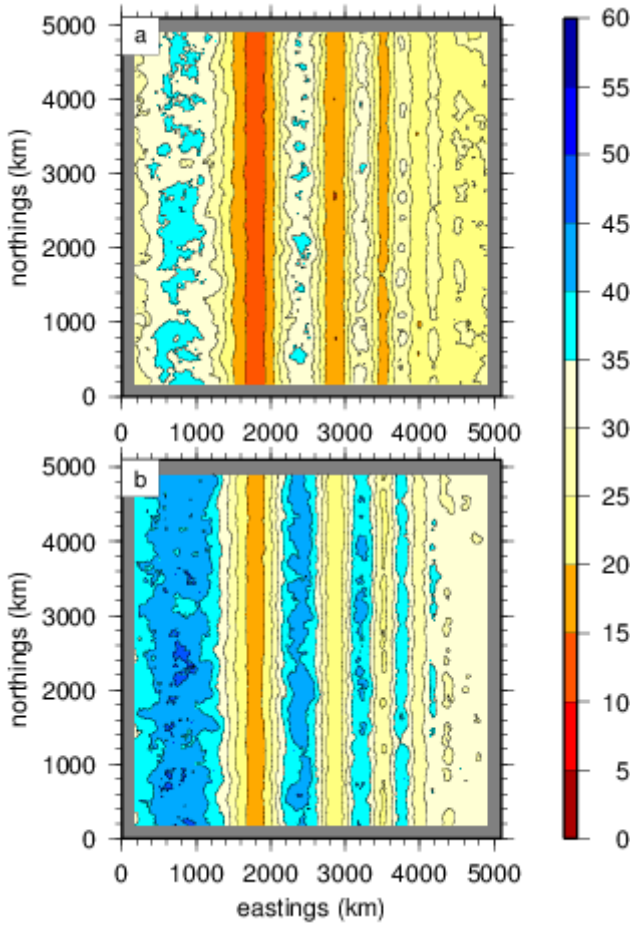

743

744 Fig. 4. T_e averaged over 100 T_e estimates recovered using the multitaper Fourier

745 transform from 100 synthetic load pairs emplaced on a plate with the T_e distribution

746 shown in Fig. 2a. Results are from deconvolution of (a) Moho relief, and (b) Bouguer

747 anomaly – see Appendix. Multitaper window size is 400×400 km, incremented every

748 20 km, with $k = NW = 3$. T_e contours at 5 km intervals.

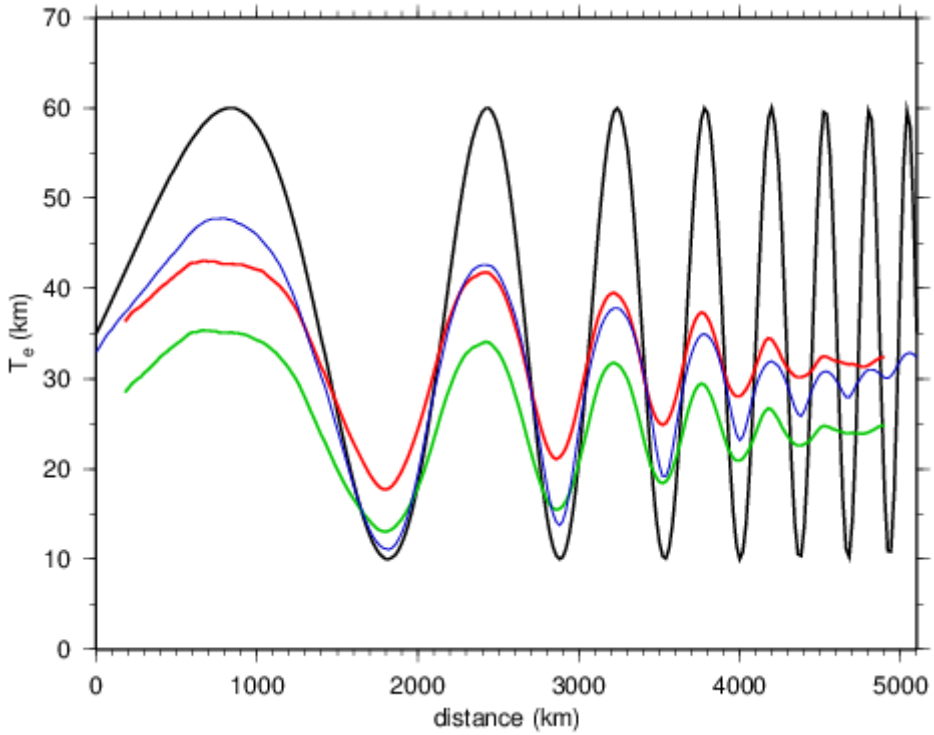

Fig. 5. Average T_e from west to east of the input T_e distribution in Fig. 2a (black), and the multitaper T_e grids in Fig. 4a (green, Moho relief deconvolution), and Fig. 4b (red, gravity deconvolution). The $|\mathbf{k}_0|$ = 2.668 wavelet cross-section from Fig. 3 is shown in blue for comparison.

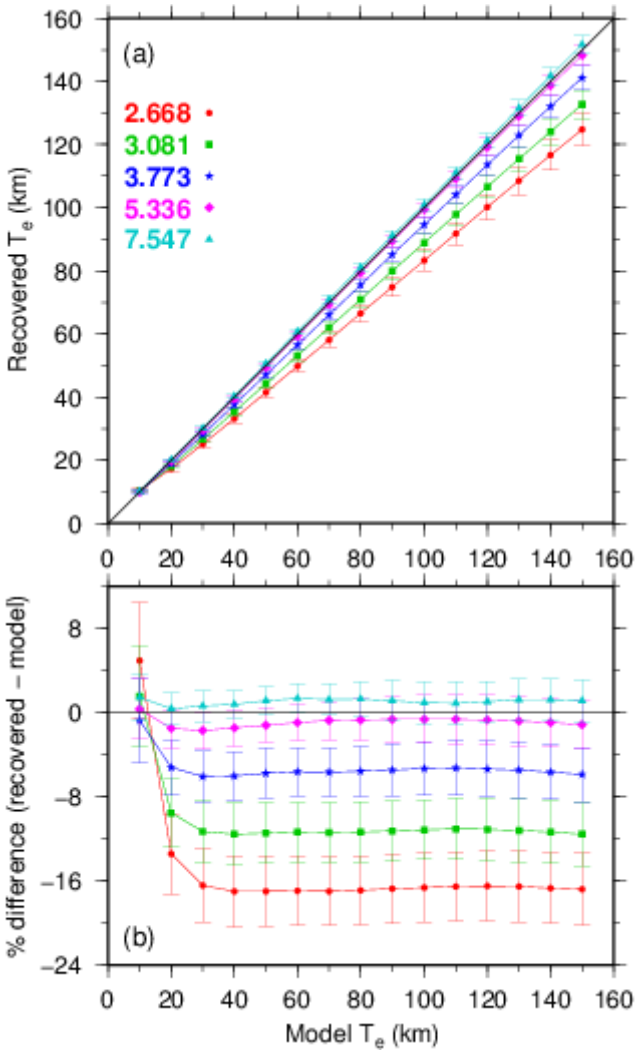

754

755 Fig. 6. Uniform-T_e recovery from the wavelet transform for the $|\mathbf{k}_0|$ values indicated in
756 (a). (a) Absolute recovered values vs input T_e of the plate. The black line shows the
757 ideal, expected relationship. (b) The difference between the average recovered and
758 model values, as a percentage of the model [= 100 ($T_e^{\text{mod}} - T_e^{\text{rec}}$) / T_e^{mod}]. Error bars
759 are one standard deviation of the percentage difference (= 100 $\sigma[T_e^{\text{rec}}]$ / T_e^{mod}, from
760 propagation of variances).

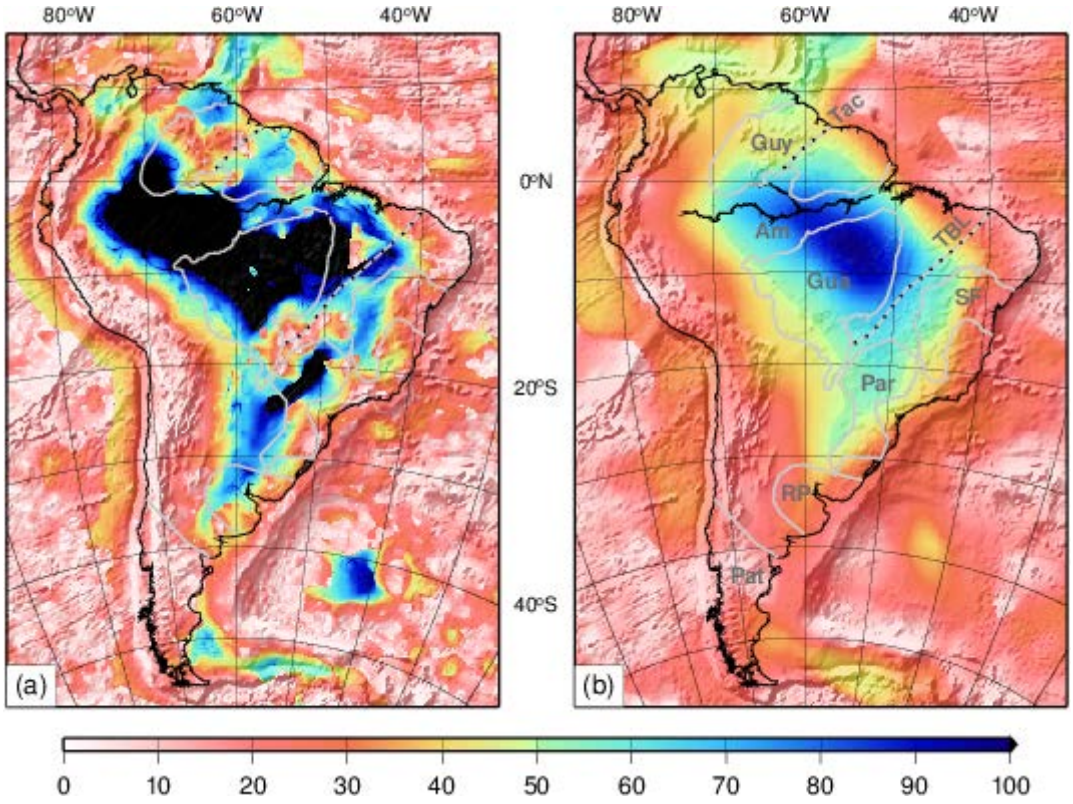

761

762 Fig. 7. T_e (in km) over South America from wavelets with $|\mathbf{k}_0|$ = (a) 2.668, and (b)
763 5.336. We inverted the Bouguer coherence using the loading model of Banks et al.
764 (2001) with the internal load placed at the interface between the upper and middle
765 crust, as given by the CRUST2.0 model (Bassin et al., 2000). Topography shaded
766 relief superimposed. Grey lines (taken from Pérez-Gussinyé et al., 2007) mark the
767 locations of the following tectonic features: the Precambrian Guyana (Guy) and
768 Guaporé (Gua) shields, which, together with the intervening Precambrian-underlain
769 Amazon basin (Am), form the Amazonian craton; Precambrian São Francisco (SF)
770 and Rio de la Plata (RP) cratons; the Precambrian-underlain Paraná basin (Par);
771 Transbrasiliano lineament (TBL); Mesozoic Tacutu rift (Tac); Phanerozoic
772 Patagonian terrane (Pat).